

# Creating Sodium Ion Channels via *De Novo* Encapsulation of Ionophores for Enhanced Water Energy Harvesting

Qing Guo, Zhiwei Xing, Huaxi Guo, Zhuozhi Lai, Jiaming Yi, Di Wu, Zhifeng Dai, Li Zhang, Sai Wang,\* Shengqian Ma, and Qi Sun\*

Biological ion channels achieve remarkable permselectivity and cation discrimination through the synergy of their intricate architectures and specialized ionophores within confined nanospaces, enabling efficient energy conversion. Emulating such selectivity in synthetic nanochannels, however, remains a persistent challenge. To address this, a novel host-guest assembly membrane is developed by incorporating sodium-selective ionophores into a  $\beta$ -ketoenamine-linked covalent organic framework (COF). This design confers exceptional permselectivity and  $\text{Na}^+$  selectivity, achieving  $\text{Na}^+/\text{K}^+$  and  $\text{Na}^+/\text{Li}^+$  selectivity ratios of 3.6 and 103, respectively, along with near-perfect  $\text{Na}^+/\text{Cl}^-$  selectivity under a 0.5 M || 0.01 M salinity gradient. Notably, the membrane dynamically switches its permselectivity to favor anion transport in the presence of high-valent cations (e.g.,  $\text{Ca}^{2+}$ ), overcoming limitations such as uphill cation diffusion and back currents observed in conventional cation-selective membranes. This adaptive behavior yields a 4.6-fold increase in output power density in  $\text{Ca}^{2+}$ -rich environments. These findings advance the design of biomimetic nanochannels with unparalleled ion selectivity and enhanced energy conversion efficiency.

## 1. Introduction

Biological ion channels exhibit remarkable efficiency in selectively transporting ions, playing pivotal roles in ion diffusion, membrane potential regulation, and bioelectric signaling.<sup>[1,2]</sup> Inspired by these natural systems, researchers have developed nanofluidic technologies that harness salinity gradients between water bodies to generate electricity.<sup>[3–7]</sup> In such systems, the performance of permselective membranes is critical for minimizing energy losses by effectively separating solutions of differing salinities.<sup>[8–20]</sup> Consequently, the design of ion-exchange membranes with high permselectivity and excellent ionic conductivity has become a key focus. However, achieving this goal is particularly challenging in complex aqueous environments, especially those containing multivalent ions like  $\text{Ca}^{2+}$ . Traditional cation-exchange membranes often favor multivalent ions, leading to increased power dissipation through back currents-ion flows from

low to high salinity regions that reduce energy conversion efficiency.<sup>[21,22]</sup> Drawing inspiration from nature's ability to exploit specific ion gradients to maintain stable potentials, membranes that combine charge selectivity with ion-specific preferences hold great promise.<sup>[23,24]</sup> Given the prevalence of  $\text{Na}^+$  ions in both natural and industrial systems, developing membranes with strong charge selectivity and high  $\text{Na}^+$  specificity of paramount importance. However, synthesizing membranes that effectively balance these properties remains a significant challenge.

Ionophores, which are compounds that facilitate selective ion transport across membranes, present a promising solution.<sup>[25–27]</sup> Integrating  $\text{Na}^+$  ionophores into membranes could enhance both  $\text{Na}^+$  selectivity and transport efficiency, thereby improving energy conversion performance. However, directly incorporating  $\text{Na}^+$  ionophores into membranes to form continuous transport pathways is challenging due to their structural complexity. Host-guest assemblies provide a versatile alternative to overcome this limitation, with applications in separation, catalysis, and beyond. By encapsulating functional species into host materials during synthesis, this approach enables the creation of innovative materials that are difficult to achieve through direct integration. In these assemblies, host

Q. Guo, Z. Xing, Z. Lai, J. Yi, D. Wu, Q. Sun  
 Zhejiang Provincial Key Laboratory of Advanced Chemical Engineering  
 Manufacture Technology  
 College of Chemical and Biological Engineering  
 Zhejiang University  
 Hangzhou 310027, China  
 E-mail: [sunqichs@zju.edu.cn](mailto:sunqichs@zju.edu.cn)

H. Guo, Z. Dai, L. Zhang  
 Key Laboratory of Surface & Interface Science of Polymer Materials of  
 Zhejiang Province  
 School of Chemistry and Chemical Engineering  
 Zhejiang Sci-Tech University  
 Hangzhou 310018, China

S. Wang  
 Hangzhou Institute of Advanced Studies  
 Zhejiang Normal University  
 Hangzhou 311231, China  
 E-mail: [wangsai@zju.edu.cn](mailto:wangsai@zju.edu.cn)

S. Ma  
 Department of Chemistry  
 University of North Texas  
 1508 W Mulberry St, Denton, TX 76201, USA

The ORCID identification number(s) for the author(s) of this article can be found under <https://doi.org/10.1002/adma.202420636>

DOI: 10.1002/adma.202420636

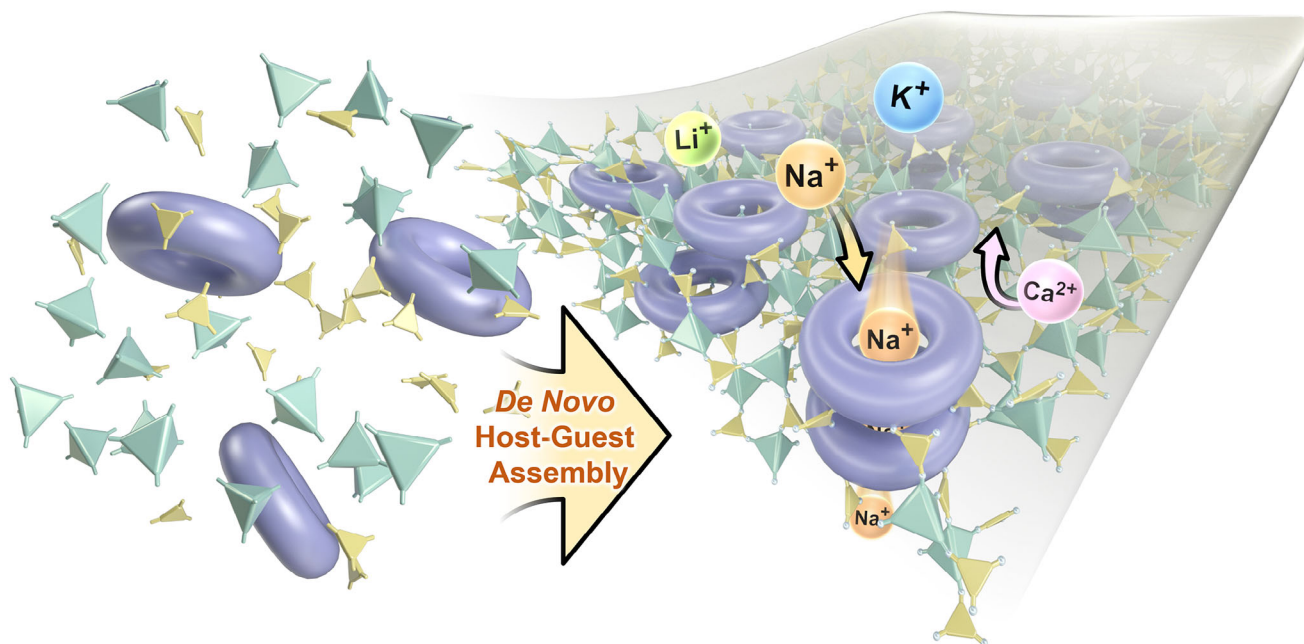


**Figure 1.** Conceptual design of integrating ionophores into COF pore channels via *de novo* host-guest assembly to enhance ion selectivity. Green and yellow elements represent the monomers used to synthesize the COF, while the purple circles represent  $\text{Na}^+$  ionophore molecules.

materials self-assemble around the guest molecules, forming porous matrices that interact synergistically with the guest species, imparting novel properties to the resulting membranes (Figure 1).<sup>[28–34]</sup>

Covalent organic frameworks (COFs) are particularly well-suited for such applications due to their tunable pore structures and versatile functionalities.<sup>[35–49]</sup> Compared to one-dimensional (1D) infiltration, three-dimensional (3D) confinement offers more effective solutions to challenges such as pore blockage by guest molecules.<sup>[50–52]</sup> Building on previous research involving two-dimensional (2D) COF membranes, which demonstrated exceptional permselectivity under high-salinity conditions through ion-dipole interactions,<sup>[53]</sup> we hypothesized that embedding  $\text{Na}^+$  ionophores into a 3D COF structure with  $\beta$ -ketoenamine linkages would enhance both permselectivity and  $\text{Na}^+$  specificity. Our results confirmed this hypothesis. The modified membrane altered the typical ion diffusion hierarchy, enabling  $\text{Na}^+$  to become the fastest-transporting ion, even surpassing  $\text{K}^+$ . It also exhibited significant cation selectivity for monovalent salts as well as anion selectivity in the presence of multivalent cations. This led to an ion-rectifying effect under asymmetric ionic conditions, reducing back currents and aligning forward currents in nanofluidic devices. These advances addressed long-standing challenges in traditional cation-exchange membranes, significantly improving energy conversion efficiency. Notably, replacing  $\text{Na}^+$ -rich water with  $\text{Ca}^{2+}$ -rich water to simulate river conditions resulted in a 4.6-fold increase in power density. These findings not only deepen our understanding of biological ion channel mechanisms but also provide a promising strategy for designing high-performance ion-selective membranes.

## 2. Results and Discussion

### 2.1. Membrane Preparation and Characterization

Prior to experimentation, we conducted density functional theory (DFT) calculations to identify potential  $\text{Na}^+$  ionophores by assessing the relative affinities of various molecules for different ions. Among the candidates, Diazine Green (DG), a positively charged molecule containing an azo group with dimensions of  $1.0 \times 2.8$  nm, showed a higher affinity for  $\text{Na}^+$  ions ( $-0.154$  eV) compared to  $\text{K}^+$  ( $-0.151$  eV) and  $\text{Li}^+$  ( $-0.071$  eV) ions (Figure 2a,b; Figure S1, Supporting Information). These results indicate that DG is a promising  $\text{Na}^+$  ionophore, capable of facilitating selective  $\text{Na}^+$  ion transport. While the binding energy difference between  $\text{Na}^+$  and  $\text{K}^+$  for a single ionophore is modest, it is crucial to consider that ions interact with multiple ionophores during transmembrane transport. This collective interaction significantly amplifies the differences in their binding affinities. This concept is analogous to how a single hydrogen bond may be weak, but the collective strength of many hydrogen bonds contributes to the stability of the DNA double helix.<sup>[54]</sup>

For the immobilization matrix in the host-guest assembly, we selected a 3D COF synthesized from tetraphenylmethaneamine (Tam) and trimethylphloroglucinol (Tp), designated COF-TamTp. This choice was made due to its ability to form COFs with chemically stable  $\beta$ -ketoenamine linkages, along with an angstrom-sized pore window of  $5.8$  Å, which effectively prevents the leaching of encapsulated  $\text{Na}^+$  ionophore molecules. DG was incorporated into the COF-TamTp membrane through *de novo* assembly. To enhance membrane processability, the COF layer was grown on a polyacrylonitrile (PAN) ultrafiltration membrane

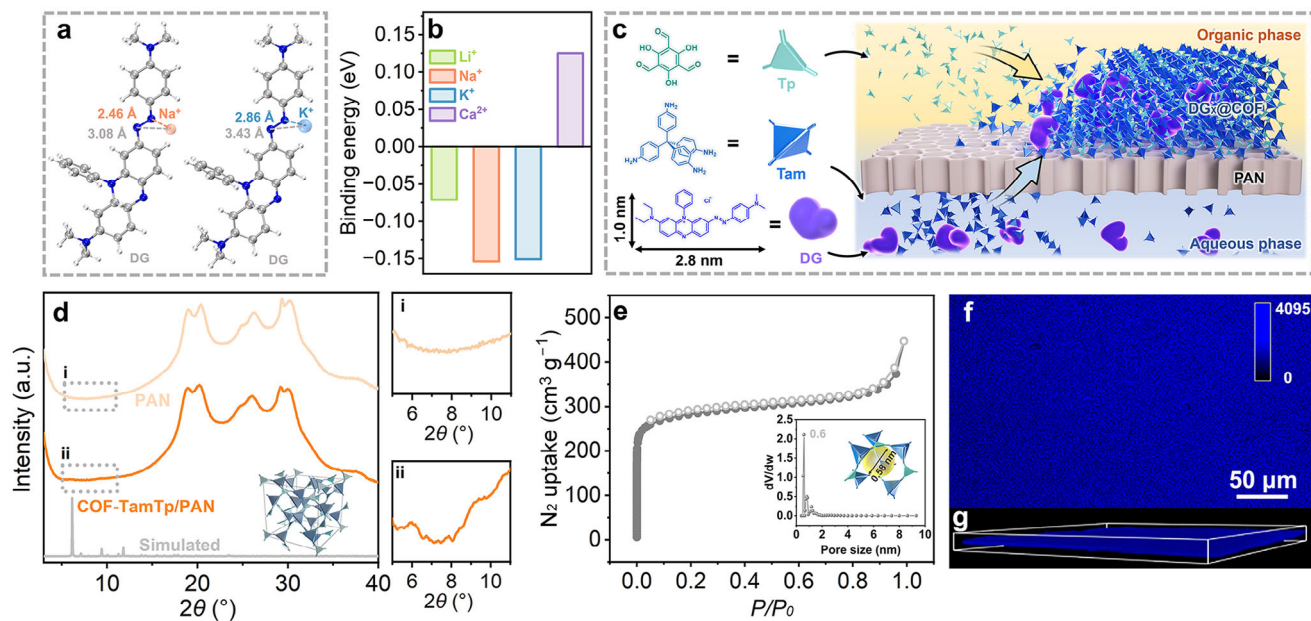


**Figure 2.** Synthesis and characterization of membranes. a, b) The optimized configurations alongside the ion binding energies. c) The synthetic scheme for the host-guest assembly, leading to the growth of the  $\text{DG}_x\text{@COF}$  membrane on the PAN support (inset: chemical structures of Tp, Tam, and DG). d) SAXS patterns, with an enlarged section and the simulated powder X-ray diffraction (PXRD) pattern based on the I-43d space group. e)  $\text{N}_2$  sorption isotherms collected at 77 K; inset displays pore size distribution determined by the non-local density functional theory (NLDFT) method and the cage dimension of COF-TamTp. f, g) CLSM images of the  $\text{DG}_{6.2}\text{@COF/PAN}$  membrane.

characterized by a uniform, finger-like pore structure (Figure 2c). This configuration facilitated the formation of a dense COF active layer while minimizing ion leakage, as confirmed by horizontal-axis testing (Figure S2, Supporting Information). During the assembly process, an organic Tp solution was placed adjacent to the PAN layer, while an aqueous solution containing Tam, DG, and acetic acid was applied to the opposite side of the nonwoven fabric. The system was maintained at 35 °C for five days to enable interfacial polymerization (Figure S3, Supporting Information). DG molecules were efficiently incorporated into the COF matrix through  $\pi$ - $\pi$  stacking interactions and electrostatic attraction between the positively charged DG molecules and the partially negatively charged oxygen atoms on the polar carbonyl groups of the COF. This was further confirmed by UV-vis spectroscopy, which showed a distinct redshift ( $\Delta\lambda = 85.6$  nm) in the characteristic absorption peak of the DG molecules, shifting from 600.7 to 686.3 nm (Figure S4, Supporting Information).<sup>[55]</sup> The resulting membranes, termed  $\text{DG}_x\text{@COF/PAN}$  (where x represents the DG concentration in  $\text{mg mL}^{-1}$  used during growth), were characterized by scanning electron microscopy (SEM), revealing compact COF membranes selectively grown on the PAN surface, with thicknesses ranging from 165 to 190 nm (Figures S5–S9, Supporting Information). The crystallinity of the COF layer was verified using small-angle X-ray scattering (SAXS), which displayed distinct diffraction peaks despite the thinness of the layer, confirming high crystallinity (Figure 2d; Figure S10, Supporting Information). The peak positions corresponded to a simulated structure with a space group of I-43d, lattice parameters  $a = b = c = 35.1651$  Å, and angles  $\alpha = \beta = \gamma = 90^\circ$  (Table S1, Supporting Information). Additionally, the Brunauer–Emmett–Teller (BET) surface area of the membrane was measured at  $855$   $\text{m}^2 \text{g}^{-1}$ , with

pore size distributions (calculated using non-local density functional theory) centered  $\approx 6.0$  Å, aligning with theoretical predictions (Figure 2e).

The encapsulation of  $\text{Na}^+$  ionophore molecules within the COF membrane is evidenced by a distinct color shift from yellow to the characteristic hue of DG (Figure S11, Supporting Information). This color change becomes more pronounced with increasing DG concentration, demonstrating that the DG loading can be precisely controlled by adjusting its solution concentration. Fourier-transform infrared (FTIR) spectroscopy further confirms both the successful formation of COF-TamTp and the immobilization of DG. The absence of aldehyde  $\text{C}=\text{O}$  ( $1634$   $\text{cm}^{-1}$ ) and primary  $\text{N}-\text{H}$  ( $3156$   $\text{cm}^{-1}$ ) stretching peaks in the FTIR spectra indicates effective condensation reactions. The appearance of ketone  $\text{C}=\text{O}$  ( $1614$   $\text{cm}^{-1}$ ) and  $\text{C}=\text{C}$  ( $1593$   $\text{cm}^{-1}$ ) peaks supports the formation of the  $\beta$ -ketoenamine-linked COF structure (Figure S12, Supporting Information). Additionally, an increase in the  $\text{C}-\text{N}$  stretching peak at  $1100$   $\text{cm}^{-1}$ , correlating with higher DG concentrations, confirms enhanced DG incorporation within the membranes (Figure S13, Supporting Information). Zeta potential measurements reveal that  $\text{DG}_x\text{@COF/PAN}$  membranes exhibit less negative potentials compared to pristine COF-TamTp/PAN membranes. This trend, which becomes more pronounced with increasing DG concentration during synthesis, indicates the progressive integration of positively charged DG molecules (Figure S14, Supporting Information). X-ray photoelectron spectroscopy (XPS) and UV-vis spectroscopy analyses of digested membrane samples were used to quantify the DG content, yielding values of 0.45, 0.51, 0.56, and 0.65  $\text{mg mg}^{-1}$  for  $\text{DG}_{1.8}\text{@COF/PAN}$ ,  $\text{DG}_{3.7}\text{@COF/PAN}$ ,  $\text{DG}_{6.2}\text{@COF/PAN}$ , and  $\text{DG}_{9.0}\text{@COF/PAN}$ , respectively. These values correspond to DG

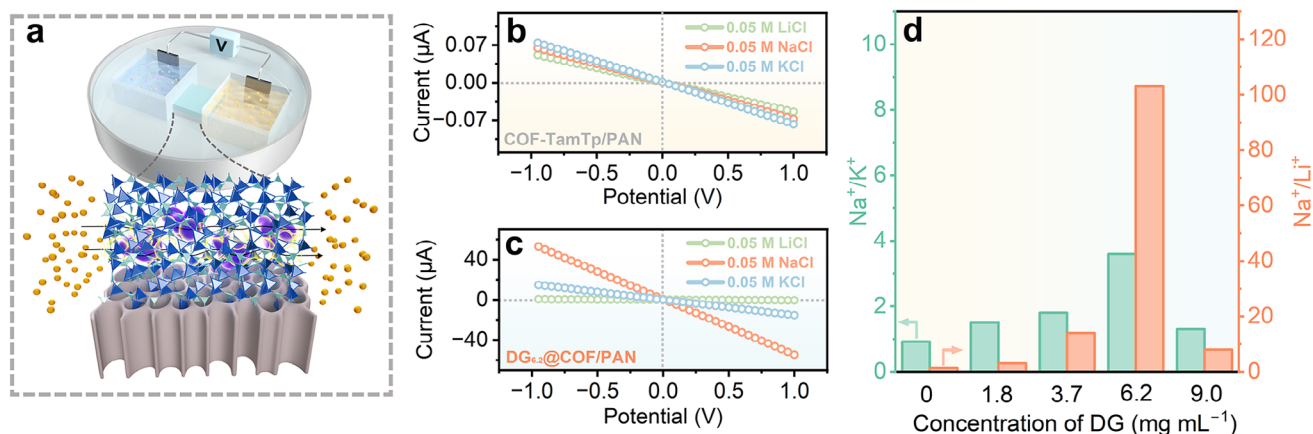


**Figure 3.** Effect of Na<sup>+</sup> ionophore content on ion transport across membranes. a) Schematic of the experimental setup used to measure ion transport across the membrane. b,c)  $I-V$  curves recorded for nanofluidic devices assembled with COF-TamTp/PAN and DG<sub>6.2</sub>@COF/PAN in various electrolytes. d) Effect of DG encapsulation content on the separation performance for Na<sup>+</sup>/K<sup>+</sup> and Na<sup>+</sup>/Li<sup>+</sup>, highlighting differences in selectivity.

molecule occupancy of 37.5%, 50.0%, 62.5%, and 87.5% of the COF membrane cavity volume (Figures S15 and S16, and Table S2, Supporting Information). Finally, confocal laser scanning microscopy (CLSM) at an excitation wavelength of 405 nm confirmed the homogeneous distribution of DG within the membrane structure, as evidenced by uniformly distributed fluorescence (Figure 2f,g; Figures S17 and S18, Supporting Information).

## 2.2. Investigation of the Impact of DG Encapsulation on Ion Transmembrane Transport Behavior

To fabricate nanofluidic devices using COF membranes, the membranes were first cut into 1.0 mm × 2.0 mm rectangular strips using a knife. These strips were then embedded in a polydimethylsiloxane (PDMS) elastomer, with reservoirs created at both ends of the membrane to allow contact with the electrolyte solution. Before testing, the assembled devices were immersed in deionized water to fully hydrate the membrane channels. Ag/AgCl electrodes were inserted into the reservoirs to establish an electrical circuit (Figure 3a). The PAN membrane alone exhibited no detectable current signal, confirming the absence of ionic leakage pathways. In contrast, the COF-layered membrane showed a stable current signal, demonstrating the effectiveness of system in studying ion transport across COF membranes (Figure S19, Supporting Information). To evaluate the impact of DG molecules on the cation selectivity of the COF-TamTp/PAN membrane, ion conductivities were measured using current-voltage ( $I-V$ ) curves in 0.05 M solutions of KCl, NaCl, and LiCl. The  $I-V$  curves displayed linear behavior consistent with Ohm's law, enabling the calculation of ion conductivities from the slopes. For the pristine COF-TamTp/PAN membrane, the ( $G$ ) conductivity sequence was  $G_{\text{KCl}} > G_{\text{NaCl}} > G_{\text{LiCl}}$ , reflecting the mobility order of the respective cations ( $\text{K}^+ > \text{Na}^+ > \text{Li}^+$ ). The introduction of DG molecules significantly enhanced Na<sup>+</sup> conductivity, altering the sequence to  $\text{Na}^+ > \text{K}^+ > \text{Li}^+$  (Figure 3b,c). Specifically,  $G_{\text{NaCl}}$  increased from 0.07  $\mu\text{S}$  in the pristine membrane to 0.51  $\mu\text{S}$  in DG<sub>1.8</sub>@COF/PAN, with a DG

content of 0.45 mg mg<sup>-1</sup>, resulting in  $G_{\text{NaCl}}/G_{\text{KCl}}$  and  $G_{\text{NaCl}}/G_{\text{LiCl}}$  ratios of 1.6 and 3.2, respectively. At a membrane DG content of 0.56 mg mg<sup>-1</sup> (DG<sub>6.2</sub>@COF/PAN),  $G_{\text{NaCl}}$  rose sharply to 54.90  $\mu\text{S}$ , with the  $G_{\text{NaCl}}/G_{\text{KCl}}$  and  $G_{\text{NaCl}}/G_{\text{LiCl}}$  ratios increasing further to 3.6 and 103. However, when the membrane DG content reached 0.65 mg mg<sup>-1</sup> (DG<sub>9.0</sub>@COF/PAN),  $G_{\text{NaCl}}$  decreased to 3.65  $\mu\text{S}$  (Figure 3d). This decline is likely due to DG molecule aggregation, which blocked ion channels and reduced selectivity, as the DG molecules occupied 87.5% of the COF membrane cavity volume. Despite this decrease, Na<sup>+</sup> conductivity remained consistently high across DG-modified membranes and various electrolyte concentrations. Notably, at a 1 M salt concentration, DG<sub>6.2</sub>@COF/PAN achieved  $G_{\text{NaCl}}/G_{\text{KCl}}$  and  $G_{\text{NaCl}}/G_{\text{LiCl}}$  ratios of 1.9 and 133, respectively (Figures S20–S23, Supporting Information). These findings highlight the role of DG as a Na<sup>+</sup> ionophore, likely by coordinating Na<sup>+</sup> ions with lone-pair electrons on nitrogen atoms in azo groups, which facilitates Na<sup>+</sup> migration through reversible coordination bonds and lowers the diffusion barrier.<sup>[56]</sup>

We then investigated the impact of DG encapsulation on membrane permselectivity, focusing on the transmembrane mobility ratio ( $\mu^+/\mu^-$ ), which represents the relative mobility of cations ( $\mu^+$ ) to anions ( $\mu^-$ ) for ions with different charges and hydrated sizes. A tenfold concentration gradient (0.1 M || 0.01 M) was applied across the membrane, and the resulting diffusion potential, driven by the differential migration rates of cations and anions, was measured. The following key observations were made using the Goldman–Hodgkin–Katz (GHK) equation: 1) The COF-TamTp/PAN membrane primarily facilitated cation transport for monovalent cation salts, with KCl showing the highest  $\mu^+/\mu^-$  ratio of 6.9. When DG molecules were introduced, cation selectivity was notably enhanced. For instance, the  $\mu^+/\mu^-$  ratio for NaCl increased from 4.1 in the pristine membrane to 16.0 in DG<sub>6.2</sub>@COF/PAN, surpassing the selectivity of other salts. 2) Both unmodified and DG-modified membranes showed a preference for anion transport for multivalent cation salts, with  $\mu^-/\mu^+$  values ranging from 1.4 to 4.0 (Figure 4a; Figure S24, Supporting Information). Notably, the DG<sub>6.2</sub>@COF/PAN membrane exhibited enhanced anion selectivity compared to the unmodified version.

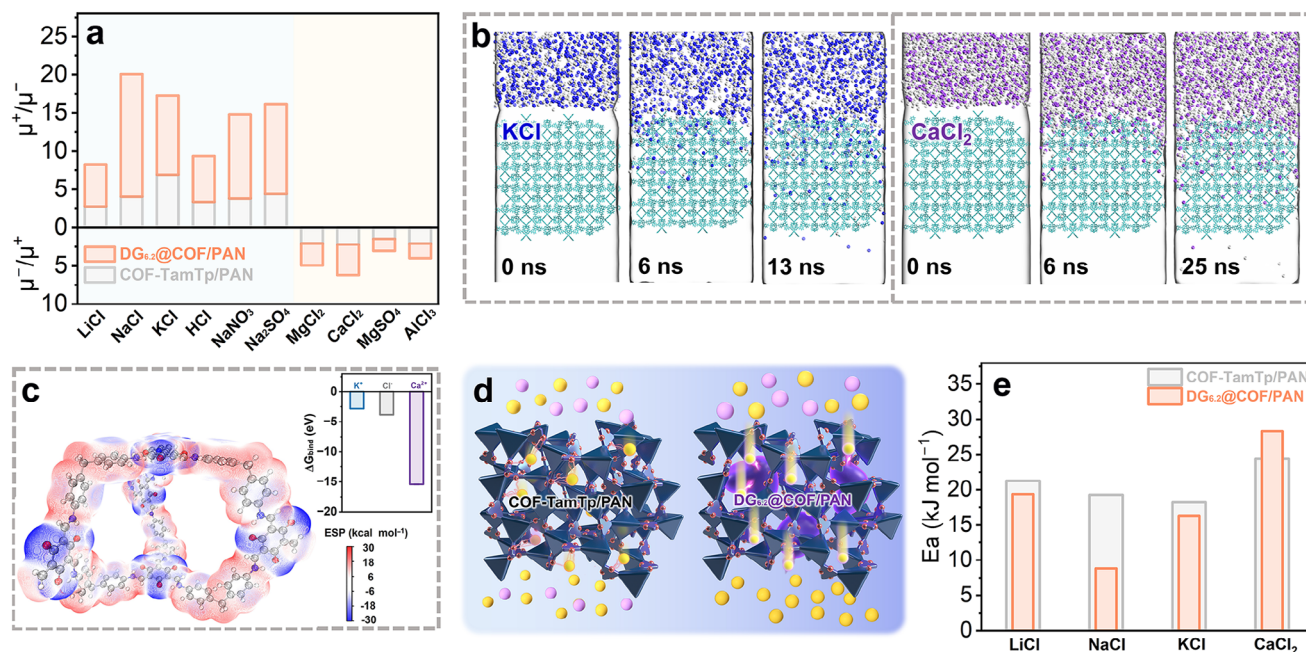


**Figure 4.** Analysis of ion transmembrane transport behavior. a) Comparison of mobility ratios for cations and anions across  $\text{DG}_{6.2}@COF/PAN$  and  $COF\text{-TamTp/PAN}$  membranes, determined using the GHK equation. b) Snapshots of  $\text{K}^+$  ions (blue), and  $\text{Cl}^-$  ions (gray), and  $\text{Ca}^{2+}$  (purple) migrating through  $COF\text{-TamTp}$  layers (cyan). c) Visualization of the molecular electrostatic potential for an individual cavity of the  $COF\text{-TamTp}$  membrane, with local minima and maxima highlighted by blue and red spheres, respectively, for clarity. Inset: Binding energies of  $\text{K}^+$ ,  $\text{Cl}^-$ , and  $\text{Ca}^{2+}$  with the  $COF$  membrane. d) Schematic illustrating  $COF$  membrane encapsulation of  $DG$  molecules to enhance ion separation. e) Comparison of apparent activation energies ( $E_a$ ) for various ions in  $\text{DG}_{6.2}@COF/PAN$  and  $COF\text{-TamTp/PAN}$  membranes.

To explore the atypical permselectivity of the  $COF\text{-TamTp/PAN}$  membrane and the improved selectivity resulting from the introduction of positively charged  $\text{Na}^+$  ionophores from  $DG$ , we conducted a control experiment by encapsulating  $DG$  molecules in  $COF\text{-300/PAN}$ . This structure, which features imine linkages formed from the condensation of Tam and terephthalaldehyde (TPA), has a pore size of 7.2 Å. Transmembrane  $\mu^+/\mu^-$  values for a range of electrolytes ( $\text{LiCl}$ ,  $\text{NaCl}$ ,  $\text{KCl}$ ,  $\text{Na}_2\text{SO}_4$ ,  $\text{CaCl}_2$ , and  $\text{MgCl}_2$ ) were measured and consistently favored anion transport, with  $\mu^+/\mu^-$  values ranging from 0.13 to 0.31. These findings highlight the significant influence of the host membrane matrix on ion selectivity (Figures S25 and S26, Supporting Information). Next, molecular dynamics (MD) simulations were performed on the  $COF\text{-TamTp}$  membrane. The MD trajectory data indicated that this electrically neutral membrane displays significant permselectivity, favoring the transport of  $\text{K}^+$  over  $\text{Cl}^-$  and  $\text{Cl}^-$  over  $\text{Ca}^{2+}$  (Figure 4b; Figures S27 and S28, Supporting Information). Electrostatic potential (ESP) calculations of the  $COF\text{-TamTp}$  matrix revealed regions of partial positive and negative charges within the cavity, resembling a dipole, promoting selective ion transport. (Figure 4c; Figure S29, Supporting Information).<sup>[57–59]</sup> Specifically, the membrane preferentially transports counter-ions over those with a higher affinity for the matrix. Binding energy ( $\Delta G_{\text{bind}}$ ) analysis further confirmed that the  $COF$  cavity binds  $\text{Cl}^-$  more strongly than  $\text{K}^+$ , and  $\text{Ca}^{2+}$  more strongly than  $\text{Cl}^-$ , which aligns with the observed selectivity for  $\text{KCl}$  (cation) and  $\text{CaCl}_2$  (anion) solutions in our experiments.

We also observed that incorporating positively charged  $DG$  molecules improved  $\text{Cl}^-$  permselectivity. For example, the  $\mu^-/\mu^+$

ratio for  $\text{CaCl}_2$  increased from 2 in the  $COF\text{-TamTp/PAN}$  membrane to 4 in the  $\text{DG}_{6.2}@COF/PAN$  membrane. To explore this effect at the molecular level, we conducted additional MD simulations to examine the influence of the positively charged  $DG$  molecules. The results revealed a significant increase in  $\text{Cl}^-$  ion transport relative to  $\text{Ca}^{2+}$  ion transport within the membrane. Specifically, the  $\text{Cl}^-/\text{Ca}^{2+}$  translocation ratio was  $\approx 1.6$  times higher than that of the  $COF\text{-TamTp}$  membrane, indicating enhanced  $\text{Cl}^-$  permselectivity (Figures S30 and S31, Supporting Information). In contrast, for monovalent cation salts, the ionophores, which had a higher affinity for monovalent cations compared to anions, enriched the cation concentration within the membrane—particularly for  $\text{Na}^+$ . This resulted in the highest increase in the  $\mu^+/\mu^-$  ratio for  $\text{NaCl}$  compared to the  $COF\text{-TamTp/PAN}$  membrane (Figure 4d).

To further investigate the observed selectivity, we analyzed the transmembrane activation energies. The relationship between conductance and temperature for four electrolytes— $\text{NaCl}$ ,  $\text{KCl}$ ,  $\text{LiCl}$ , and  $\text{CaCl}_2$ —exhibited Arrhenius-like behavior, with apparent activation energies of 8.8, 16.3, 19.4, and 28.3  $\text{kJ mol}^{-1}$ , respectively. In comparison, the  $COF\text{-TamTp/PAN}$  membrane showed activation energies of 19.3  $\text{kJ mol}^{-1}$  for  $\text{NaCl}$ , 18.2  $\text{kJ mol}^{-1}$  for  $\text{KCl}$ , 21.3  $\text{kJ mol}^{-1}$  for  $\text{LiCl}$ , and 24.4  $\text{kJ mol}^{-1}$  for  $\text{CaCl}_2$  under similar conditions. These findings confirm that the incorporation of  $DG$  molecules significantly enhances the membrane ability to transport monovalent cations, particularly  $\text{Na}^+$ , while increasing resistance to  $\text{Ca}^{2+}$  transport (Figure 4e; Figure S32, Supporting Information).

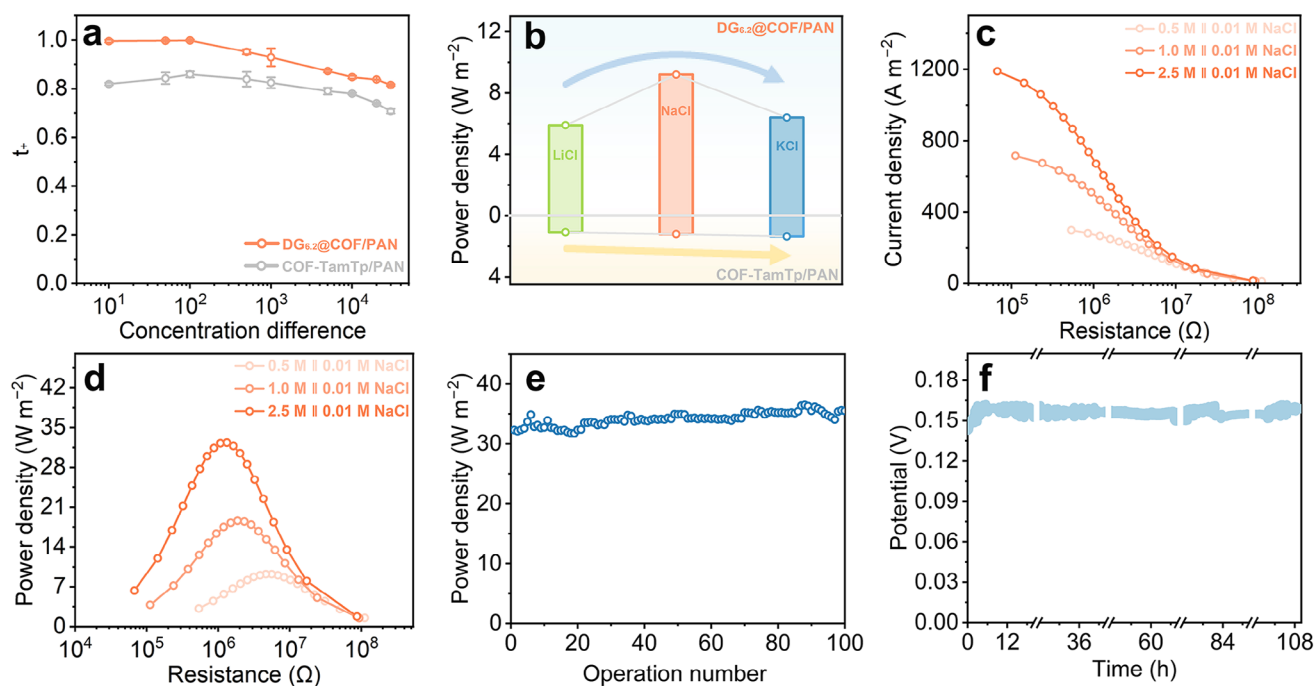


**Figure 5.** Output power density of assembled RED devices. a) Values of  $t_+$  plotted against varying NaCl concentration differences, with error bars showing the standard deviation based on three independent measurements. b) Comparison of output power densities across different electrolytes under a concentration gradient of 0.5 to 0.01 M. c,d) Graphs detailing the variation in diffusion current and power output to an external circuit across various NaCl concentration gradients. e,f) Charts depicting the operation stability over cycles and long-term stability of the open circuit voltage of the RED device assembled using DG<sub>6,2</sub>@COF/PAN with 2.5 M || 0.01 M NaCl solutions.

### 2.3. Investigation of the Impact of DG Encapsulation on Energy Conversion

Inspired by these promising results, we further investigated the charge screening capabilities of the membranes with NaCl solutions under various concentration gradients. The integration of DG molecules significantly enhances the charge selectivity of the COF-TamTp/PAN membranes, particularly at lower concentration gradients. Specifically, at NaCl gradients less than 100, the DG<sub>6,2</sub>@COF/PAN membrane achieves nearly 100% cation selectivity (as determined by the cation transference number,  $t_+$ ), whereas the COF-TamTp/PAN membrane reaches only  $\approx 80\%$  Na<sup>+</sup> selectivity. Even when the NaCl concentration gradient is as high as 30000, the DG<sub>6,2</sub>@COF/PAN membrane maintains an impressive 82% Na<sup>+</sup> ion selectivity, underscoring its potential for osmotic energy conversion (Figure 5a; Figures S33 and S34, Supporting Information).

Next, we evaluated the salinity-gradient energy conversion efficiency of various membranes using the reverse electrodialysis (RED) technique. Under a NaCl concentration gradient of 0.5 to 0.01 M, the DG<sub>6,2</sub>@COF/PAN membrane achieved a maximum output power of 9.2 W m<sup>-2</sup> with an energy conversion efficiency of 48%, approaching the theoretical maximum of 50%. This performance places it among the leading systems (Table S3, Supporting Information).<sup>[60–64]</sup> In comparison, the output power densities for KCl and LiCl under the same concentration gradients were lower, at 6.4 and 5.9 W m<sup>-2</sup>, respectively. Under similar conditions, the COF-TamTp/PAN membrane exhibited much lower output power densities: 1.21 W m<sup>-2</sup> for NaCl, 1.35 W m<sup>-2</sup> for KCl,

and 1.09 W m<sup>-2</sup> for LiCl (Figure 5b; Figure S35, Supporting Information). These results confirm that DG molecules function as Na<sup>+</sup> ionophores, enhancing the selective transmembrane transport of Na<sup>+</sup> ions. Recognizing that industrial wastewater streams often have high salt concentrations approaching saturation, we further examined the efficiency of the DG<sub>6,2</sub>@COF/PAN membrane under varying NaCl concentration gradients. Notably, at a gradient of 250 (2.5 to 0.01 M), the output power density increased significantly to 32.3 W m<sup>-2</sup> (Figure 5c,d; Figure S36, Supporting Information). Additionally, the membrane demonstrated exceptional durability, maintaining stable output power density over 100 continuous cycles (Figure 5e; Figure S37, Supporting Information). To evaluate its long-term stability, we monitored the voltage-time ( $V-t$ ) curve without altering the electrolyte. After 110 h of continuous operation, the voltage remained stable, with no significant decline, highlighting the robust and reliable performance of the DG<sub>6,2</sub>@COF/PAN membrane (Figure 5f). These results, in turn, reflect the stability of the encapsulated DG molecules during testing.

Estuaries, where seawater (predominantly NaCl) mixes with river water (rich in Ca<sup>2+</sup>), represent the largest reserves of salinity gradient energy.<sup>[65]</sup> However, traditional cation-selective membranes face significant challenges in such environments. These membranes preferentially transport multivalent cations like Ca<sup>2+</sup>, which can lead to reverse currents due to the uphill movement of Ca<sup>2+</sup> from regions of lower to higher concentration, ultimately reducing power output.<sup>[21,22]</sup> The DG<sub>6,2</sub>@COF/PAN membrane addresses this issue by exhibiting exceptional charge-based ion selectivity. It preferentially transports Na<sup>+</sup> ions in

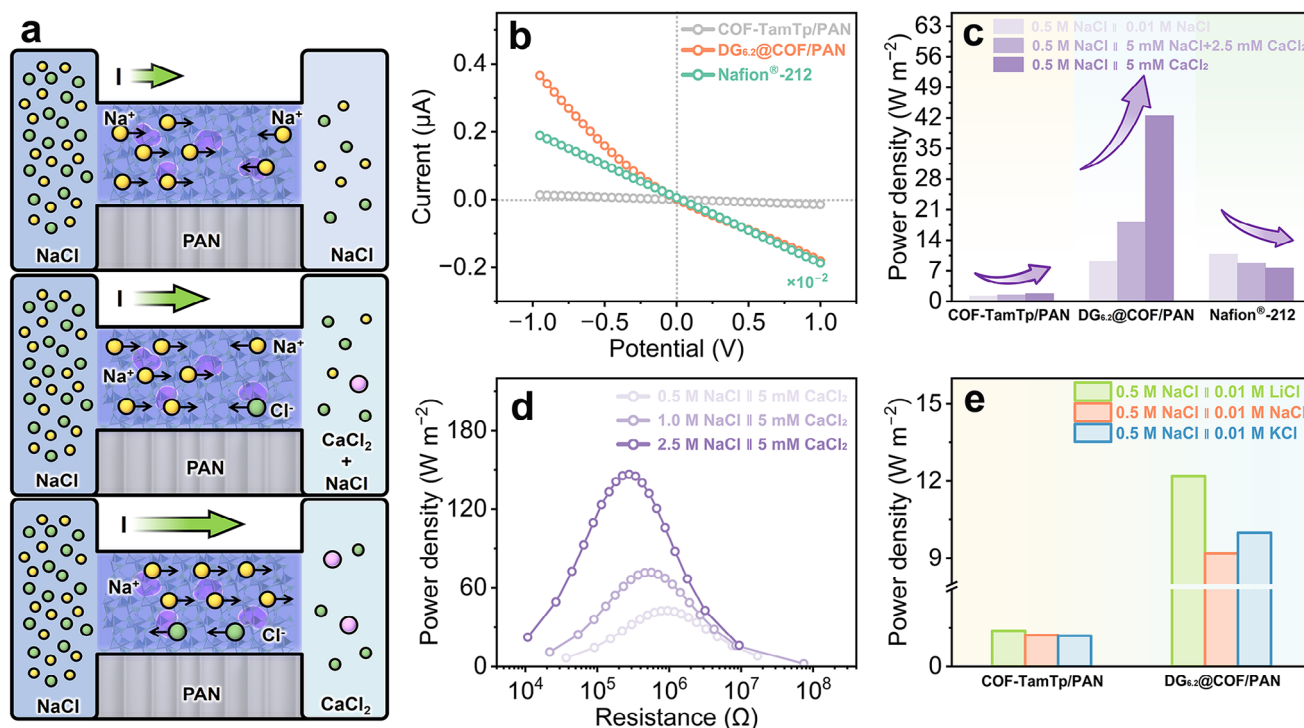


**Figure 6.** Comparison of output power density across various membranes under different ionic conditions. a) Schematic representation of ion transport directions through the DG<sub>6.2</sub>@COF/PAN membrane, showing Na<sup>+</sup> (yellow), Cl<sup>-</sup> (green), and Ca<sup>2+</sup> (pink) movement under varying ionic conditions. b) *I* – *V* curves obtained under ionic conditions of 10 mM NaCl and 5 mM CaCl<sub>2</sub>. The higher current value observed for Nafion-212 is due to its testing area being ≈52 times larger than that of the other membranes. c) Maximum output power densities achieved by various membranes under different ionic conditions. d) Power output delivered to an external circuit for DG<sub>6.2</sub>@COF/PAN under varying ionic conditions. e) Maximum output power densities across COF-TamTp/PAN and DG<sub>6.2</sub>@COF/PAN membranes tested under a range of ionic conditions.

NaCl environments and effectively selects anions in CaCl<sub>2</sub> conditions. By adjusting the ratio of Ca<sup>2+</sup> to Na<sup>+</sup> in the lower concentration solution, reverse currents can be mitigated, and in some cases, the current direction can be reversed to align with the selective ion transport, thereby enhancing power generation (Figure 6a). Our study investigates this phenomenon through *I* – *V* curve analysis under various conditions. When identical NaCl or CaCl<sub>2</sub> solutions were present on both sides of the membrane, the *I* – *V* curves were linear and passed through the origin (Figure S38, Supporting Information). However, when the membrane was placed between solutions of 10 mM NaCl and 5 mM CaCl<sub>2</sub>, with Cl<sup>-</sup> concentrations balanced, a rectifying *I* – *V* curve was observed. In contrast, the cation-selective Nafion-212 membrane exhibited a linear *I* – *V* curve under the same conditions (Figure 6b). This demonstrates the unique ion transport behavior of the DG<sub>6.2</sub>@COF/PAN membrane, which rectifies ion transport depending on the ion composition on either side of the membrane. When a forward voltage was applied to the CaCl<sub>2</sub> side (negative voltage) and reversed to the NaCl side (positive voltage), inward-rectified *I* – *V* curves were observed. The rectification ratio, defined as the current at –1 V relative to +1 V, was ≈2.4, indicating the potential for improving power generation through ion-selective transport.

To validate the practical advantages of the DG<sub>6.2</sub>@COF/PAN membrane under estuarine-like conditions, NaCl in the low-concentration solution was partially or fully replaced with CaCl<sub>2</sub>. This substitution increased output power density from 9.2 to

18.2 W m<sup>-2</sup> and 42.2 W m<sup>-2</sup> when half or all NaCl was replaced, respectively. Increasing the membrane testing area by two- and three-fold resulted in a 1.4- and 1.7-fold increase in output power, respectively. However, the output power density decreased to 71% and 56% of the original device, respectively. This reduction in power density with an increased membrane area is a common phenomenon observed in RED systems.<sup>[18]</sup>

To address this limitation, we leverage the flexible, modular design of the PDMS-encapsulated membrane. This design allows us to easily combine multiple units in series or parallel, thereby enhancing both current and voltage outputs. This flexibility enables the system to be tailored to meet varying practical requirements. For example, when five RED batteries were connected in series or parallel, the voltage and current increased by factors of 4.8 and 5.1, respectively, compared to a single RED battery (Figure S39, Supporting Information). Further increasing the NaCl concentration to 2.5 M boosted the power density to 146.5 W m<sup>-2</sup>. These results suggest that the anion-selectivity-driven current from CaCl<sub>2</sub> aligns with the Na<sup>+</sup>-selective current, resulting in synergistically enhanced power output. A similar trend was observed with the COF-TamTp/PAN membrane, where replacing half or all NaCl with CaCl<sub>2</sub> increased the power density from 1.21 to 1.46 W m<sup>-2</sup> and 1.79 W m<sup>-2</sup>, respectively. In contrast, for the cation-selective Nafion-212 membrane, power density decreased from 10.8 to 8.8 W m<sup>-2</sup> and 7.6 W m<sup>-2</sup> under the same conditions. These findings underscore the critical importance of membrane permselectivity and inter-cation

selectivity in optimizing salinity gradient power generation (Figure 6c, d; Figures S40 and S41, Supporting Information). To further illustrate the advantages of Na<sup>+</sup>-selective transport channels, the low-concentration NaCl solution was replaced with equimolar KCl or LiCl solutions. This substitution increased power density from 9.2 to 10.0 W m<sup>-2</sup> and 12.2 W m<sup>-2</sup>, respectively. The observed improvement correlated with the mobility differences between Na<sup>+</sup> and the substituted cations, highlighting the potential of leveraging industrial saline wastewater to enhance salinity gradient energy generation (Figure 6e; Figure S42, Supporting Information).

### 3. Conclusion

In this study, we successfully replicated the selective attributes of biological ion channels, achieving both inter-cation selectivity and permselectivity. This advancement effectively addresses the long-standing challenge of reduced power output in RED when using real water samples containing high-valent cations. The unique properties of the membrane arise from the interplay between the structural configuration of the host membrane and the incorporated guest ionophores. By integrating Na<sup>+</sup> ionophores, we altered the conventional ion transport hierarchy from K<sup>+</sup> > Na<sup>+</sup> > Li<sup>+</sup> to favor the transmembrane movement of Na<sup>+</sup> ions, achieving selectivities for Na<sup>+</sup>/K<sup>+</sup> and Na<sup>+</sup>/Li<sup>+</sup> of up to 3.6 and 103, respectively. This modification significantly enhanced the membrane permselectivity, achieving a Na<sup>+</sup> transference number of 0.99. This near-perfect selectivity underpins an energy conversion efficiency of 48%, approaching the theoretical maximum of 50% and setting a new benchmark for efficiency in such applications. Furthermore, the membrane exhibits adaptable permselectivity under diverse ionic conditions through ion-dipole interactions, demonstrating notable anion selectivity with divalent cation salts. This adaptability effectively mitigates the challenges posed by high-valency cations on the lower concentration side, which typically elevate back current due to uphill Ca<sup>2+</sup> transport, thereby reducing output power density. Remarkably, as the ratio of CaCl<sub>2</sub> to NaCl escalates, the output power density rises from 9.2 to 42.2 W m<sup>-2</sup> under a 50-fold salinity gradient. This pivotal finding highlights the potential for developing ion-selective nanochannels not only for salinity-gradient power generation but also for broader applications in electrochemical nanodevices.

### Supporting Information

Supporting Information is available from the Wiley Online Library or from the author.

### Acknowledgements

This work was supported by the National Key Research and Development Program of China (2024YFB3815700 and 2022YFA1503004), the National Science Foundation of China (22421004), and the National Science Foundation of Zhejiang province (LR23B060001).

### Conflict of Interest

The authors declare no conflict of interest.

### Data Availability Statement

The data that support the findings of this study are available in the supplementary material of this article.

### Keywords

covalent organic framework, energy conversion, host-guest assembly, ion permselectivity, sodium ion channel

Received: December 31, 2024

Revised: March 19, 2025

Published online: March 30, 2025

- [1] W. A. Catterall, G. Wisedchaisri, N. Zheng, *Nat. Chem. Biol.* **2020**, *16*, 1314.
- [2] T. Yang, Q. Liu, B. Kloss, R. Bruni, R. C. Kalathur, Y. Guo, E. Kloppmann, B. Rost, H. M. Colecraft, W. A. Hendrickson, *Science* **2014**, *346*, 355.
- [3] B. E. Logan, M. Elimelech, *Nature* **2012**, *488*, 313.
- [4] Z. Zhang, L. Wen, L. Jiang, *Nat. Rev. Mater.* **2021**, *6*, 622.
- [5] A. Siria, M.-L. Bocquet, L. Bocquet, *Nat. Rev. Chem.* **2017**, *1*, 0091.
- [6] K. Xiao, L. Jiang, M. Antonietti, *Joule* **2019**, *3*, 2364.
- [7] B. Zhang, W. Xu, L. Peng, Y. Li, W. Zhang, Z. Wang, *Nat. Rev. Electr. Eng.* **2024**, *1*, 218.
- [8] W. Xin, L. Jiang, L. Wen, *Angew. Chem., Int. Ed.* **2022**, *61*, 202207369.
- [9] C.-W. Chu, A. R. Fauziah, L.-H. Yeh, *Angew. Chem., Int. Ed.* **2023**, *62*, 202303582.
- [10] L. Bocquet, *Nat. Mater.* **2020**, *19*, 254.
- [11] C. Chen, D. Liu, L. He, S. Qin, J. Wang, J. M. Razal, N. A. Kotov, W. Lei, *Joule* **2020**, *4*, 247.
- [12] M. Graf, M. Lihter, D. Unuchek, A. Sarathy, J.-P. Leburton, A. Kis, A. Radenovic, *Joule* **2019**, *3*, 1549.
- [13] C. Liu, C. Ye, T. Zhang, J. Tang, K. Mao, L. Chen, L. Xue, J. Sun, W. Zhang, X. Wang, P. Xiong, G. Wang, J. Zhu, *Angew. Chem., Int. Ed.* **2024**, *63*, 202315947.
- [14] M. Macha, S. Marion, V. V. R. Nandigana, A. Radenovic, *Nat. Rev. Mater.* **2019**, *4*, 588.
- [15] X. Liu, M. He, D. Calvani, H. Qi, K. B. S. S. Gupta, H. J. M. de Groot, G. J. A. Sevink, F. Buda, U. Kaiser, G. F. Schneider, *Nat. Nanotechnol.* **2020**, *15*, 307.
- [16] Q. Liang, Y. Huang, Y. Guo, X. Zhang, X. Hu, H. Zeng, K. Liang, D. Zhao, L. Jiang, B. Kong, *Nat. Sustainability* **2024**, *7*, 628.
- [17] P. Wang, W. Tao, T. Zhou, J. Wang, C. Zhao, G. Zhou, Y. Yamauchi, *Adv. Mater.* **2024**, *36*, 2404418.
- [18] J. Yang, B. Tu, G. Zhang, P. Liu, K. Hu, J. Wang, Z. Yan, Z. Huang, M. Fang, J. Hou, Q. Fang, X. Qiu, L. Li, Z. Tang, *Nat. Nanotechnol.* **2022**, *17*, 622.
- [19] Z. Zhang, P. Bhauriyal, H. Sahabudeen, Z. Wang, X. Liu, M. Hamsch, S. C. B. Mannsfeld, R. Dong, T. Heine, X. Feng, *Nat. Commun.* **2022**, *13*, 3935.
- [20] T. Li, X. Zhang, S. D. Lacey, R. Mi, X. Zhao, F. Jiang, J. Song, Z. Liu, G. Chen, J. Dai, Y. Yao, S. Das, R. Yang, R. M. Briber, L. Hu, *Nat. Mater.* **2019**, *18*, 608.
- [21] T. Rijnaarts, E. Huerta, W. van Baak, K. Nijmeijer, *Environ. Sci. Technol.* **2017**, *51*, 13028.
- [22] D. A. Vermaas, J. Veerman, M. Saakes, K. Nijmeijer, *Energy Environ. Sci.* **2014**, *7*, 1434.
- [23] J. Li, L. Du, X. Kong, J. Wu, D. Lu, L. Jiang, W. Guo, *Natl. Sci. Rev.* **2023**, *10*, nwad260.
- [24] Q. Li, K. Zhou, B. Zhu, X. Liu, J. Lao, J. Gao, L. Jiang, *J. Am. Chem. Soc.* **2023**, *145*, 28038.

- [25] R. Quesada, *Chem* **2019**, *5*, 1924.
- [26] B. Shao, H. Fu, I. Aprahamian, *Science* **2024**, *385*, 544.
- [27] L. Zhang, J. Tian, Z. Lin, Z. Dong, *J. Am. Chem. Soc.* **2024**, *146*, 8500.
- [28] S. Chen, C. Zhu, W. Xian, X. Liu, X. Liu, Q. Zhang, S. Ma, Q. Sun, *J. Am. Chem. Soc.* **2021**, *143*, 9415.
- [29] Q. Guo, Z. Lai, X. Zuo, W. Xian, S. Wu, L. Zheng, Z. Dai, S. Wang, Q. Sun, *Nat. Commun.* **2023**, *14*, 6702.
- [30] J. Lu, G. Jiang, H. Zhang, B. Qian, H. Zhu, Q. Gu, Y. Yan, J. Z. Liu, B. D. Freeman, L. Jiang, H. Wang, *Sci. Adv.* **2023**, *9*, abq1369.
- [31] P. Liu, F. Fang, L. O. Alimi, B. A. Moosa, X. Zhu, X. Liu, H. Wang, N. M. Khashab, *Chem* **2024**, *10*, 3184.
- [32] S. Hong, M. D. Vincenzo, A. Tiraferri, E. Bertozzi, R. Górecki, B. Davaasuren, X. Li, S. P. Nunes, *Nat. Commun.* **2024**, *15*, 3160.
- [33] R. Ou, H. Zhang, V. X. Truong, L. Zhang, H. M. Hegab, L. Han, J. Hou, X. Zhang, A. Deletic, L. Jiang, G. P. Simon, H. Wang, *Nat. Sustainability* **2020**, *3*, 1052.
- [34] T. Xu, B. Wu, W. Li, Y. Li, Y. Zhu, F. Sheng, Q. Li, L. Ge, X. Li, H. Wang, T. Xu, *Sci. Adv.* **2024**, *10*, adn0944.
- [35] W. Xian, D. Wu, Z. Lai, S. Wang, Q. Sun, *Acc. Chem. Res.* **2024**, *57*, 1973.
- [36] C. S. Diercks, O. M. Yaghi, *Science* **2017**, *355*, aal1585.
- [37] K. Geng, T. He, R. Liu, S. Dalapati, K. T. Tan, Z. Li, S. Tao, Y. Gong, Q. Jiang, D. Jiang, *Chem. Rev.* **2020**, *120*, 8814.
- [38] S. Kandambeth, K. Dey, R. Banerjee, *J. Am. Chem. Soc.* **2019**, *141*, 1807.
- [39] Y. Zhang, H. Wang, W. Wang, Z. Zhou, J. Huang, F. Yang, Y. Bai, P. Sun, J. Ma, L. E. Peng, C. Y. Tang, L. Shao, *Matter* **2024**, *7*, 1406.
- [40] S. Zhao, C. Jiang, J. Fan, S. Hong, P. Mei, R. Yao, Y. Liu, S. Zhang, H. Li, H. Zhang, C. Sun, Z. Guo, P. Shao, Y. Zhu, J. Zhang, L. Guo, Y. Ma, J. Zhang, X. Feng, F. Wang, H. Wu, B. Wang, *Nat. Mater.* **2021**, *20*, 1551.
- [41] C. Kang, Z. Zhang, S. Kusaka, K. Negita, A. K. Usadi, D. C. Calabro, L. S. Baugh, Y. Wang, X. Zou, Z. Huang, R. Matsuda, D. Zhao, *Nat. Mater.* **2023**, *22*, 636.
- [42] A. Knebel, J. Caro, *Nat. Nanotechnol.* **2022**, *17*, 911.
- [43] Y. Yang, B. Liang, J. Kreie, M. Hamsch, Z. Liang, C. Wang, S. Huang, X. Dong, L. Gong, C. Liang, D. Lou, Z. Zhou, J. Lu, Y. Yang, X. Zhuang, H. Qi, U. Kaiser, S. C. B. Mannsfeld, W. Liu, A. Götzhäuser, Z. Zheng, *Nature* **2024**, *630*, 878.
- [44] J. Liu, S. Wang, T. Huang, P. Manchanda, E. Abou-Hamad, S. P. Nunes, *Sci. Adv.* **2020**, *6*, abb3188.
- [45] A. M. Evans, L. R. Parent, N. C. Flanders, R. P. Bisbey, E. Vitaku, M. S. Kirschner, R. D. Schaller, L. X. Chen, N. C. Gianneschi, W. R. Dichtel, *Science* **2018**, *361*, 52.
- [46] H. Wang, Z. Zeng, P. Xu, L. Li, G. Zeng, R. Xiao, Z. Tang, D. Huang, L. Tang, C. Lai, D. Jiang, Y. Liu, H. Yi, L. Qin, S. Ye, X. Ren, W. Tang, *Chem. Soc. Rev.* **2019**, *48*, 488.
- [47] K. Wang, H. Yang, Z. Liao, S. Li, M. Hamsch, G. Fu, S. C. B. Mannsfeld, Q. Sun, T. Zhang, *J. Am. Chem. Soc.* **2023**, *145*, 5203.
- [48] S. Yuan, X. Li, J. Zhu, G. Zhang, P. V. Puyvelde, B. V. der Bruggen, *Chem. Soc. Rev.* **2019**, *48*, 2665.
- [49] L. Cao, C. Chen, S. An, T. Xu, X. Liu, Z. Li, I.-C. Chen, J. Miao, G. Li, Y. Han, Z. Lai, *J. Am. Chem. Soc.* **2024**, *146*, 21989.
- [50] X. Guan, F. Chen, Q. Fang, S. Qiu, *Chem. Soc. Rev.* **2020**, *49*, 1357.
- [51] B. Gui, G. Lin, H. Ding, C. Gao, A. Mal, C. Wang, *Acc. Chem. Res.* **2020**, *53*, 2225.
- [52] T. Zhu, Y. Kong, B. Lyu, L. Cao, B. Shi, X. Wang, X. Pang, C. Fan, C. Yang, H. Wu, Z. Jiang, *Nat. Commun.* **2023**, *14*, 5926.
- [53] S. Yin, J. Li, Z. Lai, Q.-W. Meng, W. Xian, Z. Dai, S. Wang, L. Zhang, Y. Xiong, S. Ma, Q. Sun, *Nat. Commun.* **2024**, *15*, 8137.
- [54] Y. Liu, L. Wang, L. Zhao, Y. Zhang, Z.-T. Li, F. Huang, *Chem. Soc. Rev.* **2024**, *53*, 1592.
- [55] X. Tang, K. Zhang, R. Xue, Y. Zheng, S. Chen, S. Zheng, J. Fan, Y. Zhang, W. Ye, W. Zhang, S. Cai, Y. Liu, *Angew. Chem., Int. Ed.* **2024**, *63*, 202413171.
- [56] Y. Zhu, H. Wong, W. Zhang, *Chem. Mater.* **2013**, *25*, 1630.
- [57] E. Y. Kim, M. Mohammadiroudbari, F. Chen, Z. Yang, C. Luo, *ACS Nano* **2024**, *18*, 4159.
- [58] C. Luo, O. Borodin, X. Ji, S. Hou, K. J. Gaskell, X. Fan, J. Chen, T. Deng, R. Wang, J. Jiang, C. Wang, *Proc. Natl. Acad. Sci. USA* **2018**, *115*, 2004.
- [59] C. Yin, Z. Li, D. Zhao, J. Yang, Y. Zhang, Y. Du, Y. Wang, *ACS Nano* **2022**, *16*, 14178.
- [60] L. Ding, D. Xiao, Z. Lu, J. Deng, Y. Wei, J. Caro, H. Wang, *Angew. Chem., Int. Ed.* **2020**, *59*, 8720.
- [61] L. Cao, I.-C. Chen, C. Chen, D. B. Shinde, X. Liu, Z. Li, Z. Zhou, Y. Zhang, Y. Han, Z. Lai, *J. Am. Chem. Soc.* **2022**, *144*, 12400.
- [62] D. Huang, K. Zou, Y. Wu, K. Li, Z. Zhang, T. Liu, W. Chen, Z. Yan, S. Zhou, X.-Y. Kong, L. Jiang, L. Wen, *J. Am. Chem. Soc.* **2024**, *146*, 16469.
- [63] J. Tang, Y. Wang, H. Yang, Q. Zhang, C. Wang, L. Li, Z. Zheng, Y. Jin, H. Wang, Y. Gu, T. Zuo, *Nat. Commun.* **2024**, *15*, 3649.
- [64] C. Zhu, L. Xu, Y. Liu, J. Liu, J. Wang, H. Sun, Y.-Q. Lan, C. Wang, *Nat. Commun.* **2024**, *15*, 4213.
- [65] J. D. Hem, *Department of the Interior, US Geological Survey* **1985**, 2254.